Article:

Cyprych, D, Piazolo, SC orcid.org/0000-0001-7723-8170 and Almqvist, BSG (2017) Seismic anisotropy from compositional banding in granulites from the deep magmatic arc of Fiordland, New Zealand. Earth and Planetary Science Letters, 477. pp. 156-167. ISSN 0012-821X

https://doi.org/10.1016/j.epsl.2017.08.017

Title: Seismic anisotropy from compositional banding in granulites from the deep magmatic arc of Fiordland, New Zealand

Authors: Daria Cyprych[a], Sandra Piazolo[a,b], Bjarne S.G. Almqvist[c]

Affiliations:

[a] Australian Research Council of Excellence for Core to Crust Fluid Systems/GEMOC, Department of Earth and Planetary Sciences, Macquarie University, NSW 2109, Australia; daria.cyprych@students.mq.edu.au

[b] School of Earth and Environment, University of Leeds, United Kingdom; S.Piazolo@leeds.ac.uk

[c] Department of Earth Sciences, Uppsala University, Sweden; bjarne.almqvist@geo.uu.se

Abstract

We present calculated seismic velocities and anisotropies of mafic granulites and eclogites from the Cretaceous deep lower crust (~40-65 km) of Fiordland, New Zealand. Both rock types show a distinct foliation defined by cm-scale compositional banding. Seismic properties are estimated using the Asymptotic Expansion Homogenisation – Finite Element (AEH-FE) method that, unlike the commonly used Voigt-Reuss-Hill homogenisation, incorporates the phase boundary network into calculations. The predicted mean P- and S-wave velocities are consistent with previously published data for similar lithologies from other locations (e.g., Kohistan Arc), although we find higher than expected anisotropies (AV_P ~5.0-8.0 %, AV_S ~ 3.0-6.5 %) and substantial S-wave splitting along foliation planes in granulites. This seismic signature of granulites results from a density and elasticity contrast between cm-scale pyroxene ± garnet stringers and plagioclase matrix rather than from crystallographic orientations alone. Banded eclogites do not show elevated anisotropies as the contrast in density and elastic constants of garnet and pyroxene is too small. The origin of compositional banding in Fiordland granulites is primarily magmatic and structures described here are expected to be typical for the base of present day magmatic arcs. Hence, we identify a new potential source of anisotropy within this geotectonic setting.

1. Introduction

The seismic properties of rocks are a major source of information that is used by geologist and geophysicists to derive the composition, structure and, with that, rheology of the crust and the mantle. In particular, the directionally dependent propagation of seismic waves, i.e. seismic anisotropy, can provide valuable information about flow related structures at depth. For example, anisotropy attributed to the crystallographic preferred orientation (CPO) of olivine provides strong evidence for ductile flow within the upper mantle (Karato and Wu, 1993). Due to the very limited number of outcrops of pristine lower crustal rocks not affected by later retrogression, analysis of seismic anisotropy is also one of the prime methods to decipher the deformation behaviour of the lower crust (Moschetti et al., 2010). Seismic anisotropy can be determined using various methods, for example, P-wave and S-wave tomography (Cheng et al., 2016), and ambient noise tomography (Moschetti et al., 2010). However, the interpretation of such data is still challenging due to compositional and structural heterogeneity of the lower crust. The link between the variety of compositions and microstructures in lower crustal rocks and their seismic properties still needs to be established.

In many studies, it has been shown that seismic anisotropy in the crust can result from the presence of horizontal layering (Backus, 1962) and a strong texture or CPO of anisotropic minerals, such as amphibole and mica, which is often also associated with shape preferred orientation of these minerals in the rock mass (SPO; e.g. mica foliation, amphibole lineation) (e.g., Baker and Carter, 1972; Mainprice and Nicolas, 1989). However, besides crystallographic and shape preferred orientations many rocks exhibit compositional banding at the mm- to cm-scale which theoretically could significantly influence seismic wave propagation. Examples of such common compositional banding include mineral banding in high grade rocks, e.g. granulites, eclogites and gneisses. As compositional banding is a priori an anisotropic feature in the rock, it may result in seismic anisotropy. However, so far the influence of compositional banding, other than mica foliation, has not been studied in detail.

In this contribution we present the calculated seismic properties of rocks collected from the Cretaceous Fiordland arc (New Zealand). Interpreted to be the rapidly uplifted mafic root of a magmatic arc, this section of lower crustal rocks is relatively unaffected by later retrogression and reworking. Samples include a suite of garnet and two-pyroxene granulites with layers and pods of eclogite that represent the deep (~40-65 km) root of the arc (e.g., Clarke et al., 2013). Both analysed rock types are characterized by cm-scale compositional banding. We utilize the EBSD GUI software (Naus-Thijssen et al., 2011; Vel et al., 2016) to calculate seismic properties of the samples. Unlike previous studies on similar lithologies, velocities calculated using the EBSD GUI are based not only on elastic properties, crystallographic orientation data, and volume percent of constituent phases, but also encompass phase boundaries allowing the analysis of the impact of cm-scale banding on the seismic properties of examined rocks.

We show that for rocks composed of minerals with contrasting density and elastic constants, such as granulites, mineral banding has a marked influence on the seismic signal. Our dataset provides a range of seismic properties that adds to our ability of utilizing seismic techniques to characterize the compositional and structural nature of present-day lower crust.

2. Geological setting and sample description

The rocks exposed in Fiordland represent a continental margin of Gondwana prior to Late Cretaceous (Mortimer et al., 2006). Fiordland rocks include Median Batholith that formed in a Cordilleran-style magmatic arc setting during the Devonian - Early Cretaceous (Mortimer et al., 2006). The Median Batholith comprises Jurassic and older rocks that accreted onto Gondwana (eastern part) and Early Cretaceous plutons (western part) collectively referred to as Western Fiordland Orthogneiss (WFO). The samples collected for this study are representative for two large intrusions of the WFO: Breaksea Orthogneiss and Malaspina Pluton. These plutons form the root of the Fiordland Magmatic Arc and preserved some of the oldest and deepest igneous structures of the WFO (Klepeis et al., 2016). Samples were collected along two high ridge transects; north of Mt. Clerk, SE Resolution Island, and at Breaksea Tops between Breaksea Sound and Coal River (Fig. 1).

The Breaksea Orthogneiss (Breaksea Tops locality) was emplaced at depths of >65 km (1.8-2.0 GPa; De Paoli et al., 2009; Clarke et al., 2013) between 124-122 Ma (Milan et al., 2016). The Malaspina Pluton intruded the Breaksea Orthogneiss at shallower depths of 40-50 km (~1.4 GPa; Allibone et al., 2009) mostly between 118 and 114 Ma (Klepeis et al., 2016; Milan et al., 2016). The Breaksea Orthogneiss comprises an omphacite-garnet granulite of monzodioritic composition with layers and pods of garnet-omphacite adcumulate (eclogite; De Paoli et al., 2009), cognate inclusions of omphacite-orthopyroxenite (Chapman et al., 2015), and minor garnetite, pyroxenite, harzburgite, and pargasite peridotite (Allibone et al., 2009; Clarke et al., 2013). The Malaspina pluton at Mt. Clerke is composed of dominant garnet diopside granulite of monzodioritic composition with layers and pods of diopside-orthopyroxene granulite, garnet pyroxenite, and hornblendite (Allibone et al., 2009; Chapman et al., 2016).

Granulites from both locations show foliation (S_1) defined by shape preferred orientation of pyroxenes ± garnet stringers within a plagioclase matrix (Fig. 2a, e). Similarly, eclogites show compositional banding of clinopyroxene and garnet (Fig. 2g), parallel to S_1 (e.g., Fig. 3d of De Paoli et al., 2009). The S_1 foliation in granulites initially originated from magmatic flow (De Paoli et al., 2009; Klepeis et al., 2016) and was only weakly affected by the second tectonic event (D_2), which occurred after emplacement of the main igneous bodies and at lower crustal conditions (Klepeis et al., 2016). The magmatic mineral assemblages partially recrystallized during D_2 (Clarke et al., 2013; Chapman et al., 2016). The Breaksea Orthogneiss underwent granulite to eclogite facies metamorphism and partial melting (P~ 1.8 to 1.4 GPa, T~850 °C) at 114-93 Ma (De Paoli et al., 2009) and Malaspina pluton was subject to granulite facies metamorphism and partial melting (P~1.2-1.4 GPa, T~850-900 °C) at 116-11 Ma (Stowell et al., 2014). The mineral assemblages in the studied areas were not affected during subsequent exhumation and retrogressive, amphibolite facies metamorphism (Klepeis et al., 2016).

3. Analytical methods

3.1 Petrology, mineral chemistry and orientation data

We used polished thin and thick sections cut perpendicular to the foliation (XY) and parallel to the lineation (X). Polarized light-microscopy was used to determine the general characteristics of rock microstructure, including grain size, grain shape, phase distribution, and general deformation structures.

Full quantitative crystallographic orientation data were collected using automatically indexed EBSD patterns acquired with a HKL NordleysNano high sensitivity EBSD detector and indexed using the Aztec analysis software (Oxford instruments). The analysed area of each thin section was larger than 1 cm^2. The step size was between 10 and 15 µm. Mineral phases were distinguished based on their crystallographic characteristic and chemical composition determined using Scanning Electron Microscopy (SEM) utilizing Energy Dispersive Spectrometry (EDS) on a Zeiss IVO SEM with an X-Max EDS detector. Grain boundaries were defined by misorientations ≥10 ° between adjacent points. The detailed description of data processing can be found in Appendix A. EBSD maps are reported in Appendix B.

Crystallographic orientation data for most abundant minerals are shown in equal area, lower hemisphere pole figures and include all data points acquired during EBSD analysis. In the following we describe in detail textures of major minerals of analysed rocks based on one, most representative sample of each lithology. All textures of major minerals of analysed samples are presented in Appendix C.

For a quantitative measure of the relative strength of texture of each mineral the J-index (Bunge, 1982) of the orientation distribution functions (ODFs) derived from all data points was calculated using mTex (http://mtex-toolbox.github.io/; Hielscher and Schaeben, 2008). By definition, the J-index ranges from unity (corresponding to a completely random texture) to infinity (a single-crystal texture). Seismic properties are calculated based on textures of constituent minerals that were obtained from all orientation points acquired during EBSD mapping, as seismic waves travel through the volume of the sample. In the aggregate with a non-uniform grain size, a texture calculated using all orientation data points may be strongly influenced by the orientations of larger grains. Similarly though, if large grains exist they will affect the seismic signal to the same extent. Thus, for the purpose of comparing the texture and seismic signal it is appropriate to represent and quantify texture using all orientation data points. Furthermore, the effect of large grains is in our case minimized by the size of analysed areas, small analysis step size, and relatively fine grain size of all the minerals except garnet.

3.2 Calculation of seismic properties

To calculate seismic velocities we utilize EBSD GUI (Naus-Thijssen et al., 2011; Vel et al., 2016). To derive seismic wave speeds the software applies Christoffel's equation (Christoffel, 1877)

$$\left[C_{ijkl}^{H} n_j n_l - \rho^H V^2 \delta_{ik}\right] a_k = 0$$

in which C_{ijkl}^{H} represent the bulk homogenised stiffness matrix, n_i defines the propagation direction, ρ^H is homogenised (average) density, V is wave speed, δ_{ij} is Kronecker delta, and a_i are displacement amplitudes. The equation allows calculation of phase velocities and polarization of seismic waves based on the specified bulk homogenised stiffness matrix C_{ijkl}^{H}. To obtain the bulk homogenised stiffness matrix of polycrystalline rocks, an averaging scheme is needed that relates the average elastic strain to average elastic stress of each mineral in the rock mass. In case of an aggregate with a CPO, the anisotropy of the elastic properties of each mineral must be taken into account, and for each crystallographic orientation the single-crystal properties are rotated (Mainprice and Nicolas, 1989). Bulk elastic stiffnesses are calculated using the Voigt-Reuss-Hill (VRH) homogenisation (Voigt, 1928; Reuss, 1929; Hill, 1952) that averages the elastic properties of the constitutive minerals based on their percent area. However, seismic velocities are also affected by the grain to grain and phase to phase interactions, as these interactions result in heterogeneous stress and strain fields in minerals (Vel et al., 2016). Therefore, using EBSD GUI we discretise the 2D spatial distribution of the different phases and the boundaries between phases using the asymptotic expansion homogenisation (AEH) method combined with finite element (FE) meshing (Naus-Thijssen et al., 2011; Vel et al., 2016 and references therein). The 2D phase boundaries are projected infinitely into the third dimension (Naus-Thijssen et al., 2011; Vel et al., 2016). All in all, the AEH-FE modifies the bulk homogenised stiffness matrix C^{H}_{ijkl} allowing computing the elastic interactions between different minerals.

In the following, we calculate seismic velocities using two methods: (1) applying the VRH average and (2) applying the AEH-FE method (for simplicity, further referred to as "AEH"). We take into account minerals with abundances higher than 1 percent area. Elastic properties of minerals that represent solid solutions (such as garnets, and pyroxenes) vary depending on the chemical composition of the solid solution. Therefore, we used elastic constants of minerals with compositions that were comparable to previously published mineral chemistry for the Breaksea Orthogneiss and the Malaspina Pluton (De Paoli et al., 2009; Clarke et al., 2013; Chapman et al., 2015). Consequently, we used single-crystal stiffnesses of Bhagat et al. (1992) for omphacite (density ρ=3.33 g/cm^3), Chai et al. (1997) for garnet (ρ=3.81 g/cm^3), Collins and Brown (1998) for diopside (ρ=3.33 g/cm^3), Jackson et al. (2007) for enstatite (ρ=3.2 g/cm^3), Brown et al. (2006) for plagioclase (ρ=2.68 g/cm^3), Aleksandrov and Ryzhova (1962) for K-feldspar, Lakshtanov et al. (2007) for quartz, Weidner and Ito (1985) for ilmenite, Wachtman Jr et al. (1962) for rutile, and Sha et al. (1994) for apatite. Elastic stiffness of pargasite was approximated with those of hornblende (Aleksandrov and Ryzhova, 1961).

Mean V_P is defined as $MV_P = (V_{Pmax} + V_{Pmin})/2$, and mean V_S as $MV_S = (V_{S1max} + V_{S2min})/2$. Since the elastic constants of minerals that were used were obtained at room pressure and temperatures, our results represent seismic properties of crack-free rocks at ambient conditions. However, for most studies to date, seismic properties of lower crustal rocks have been measured in the laboratory on natural samples. Natural samples often contain microcracks that tend to reduce elastic wave velocities in general. Furthermore, aligned microcracks may lead to an increase in seismic anisotropy, which is not representative of the rock anisotropy at depth in the crust, where pressures are too high for the cracks to stay open (e.g., Siegesmund et al., 1991). Laboratory measurements are therefore usually performed at elevated pressures to close pores and microcracks to reduce their effect on P- and S-wave velocities, as well as on anisotropy. To compare our results with the previously published results obtained through laboratory measurements at confining pressure of 600 MPa, we recalculated mean V_P and mean V_S to 600 MPa pressure following the approach of Abers and Hacker (2016). Seismic anisotropy is defined as $A = 100[(V_{max}-V_{min})/(V_{max}+V_{min})/2)]$, where V_{max}, V_{min} are the maximum and minimum velocities of either P-, S-, S_1-, or S_2-wave at room pressure and temperature. The density of the rock is calculated by averaging single-crystal densities according to the area percent of the phases. To visualize anisotropy and velocity distribution, and S-wave polarization planes in sample reference frame, we used the MATLAB Seismic Anisotropy Toolkit (MSAT; Walker and Wookey, 2012). In the following, for simplicity, we focus on seismic properties of one, most representative sample of each lithology. Seismic properties of all the samples are presented in Appendix D.

4. Results

4.1. General rock composition and microstructures

Samples of granulites comprise six garnet-omphacite granulites from Breaksea Tops (BS-samples), three garnet-diopside granulites and two diopside-orthopyroxene granulites (henceforth called two-pyroxene granulites) from Resolution Island (RS-samples). Three samples of eclogite were collected from Breaksea Tops.

Garnet granulites from both study areas are composed predominantly of plagioclase, clinopyroxene, garnet, and K-feldspar, with minor quartz and pargasite, and accessory apatite and rutile (Table 1, Fig. 2a-d). Granulites from Breaksea Tops and Resolution Island comprise omphacite and diopside, respectively. Two-pyroxene granulites from Resolution Island consist of plagioclase, enstatite, diopside, K-feldspar, minor quartz and pargasite, and accessory ilmenite (Table 1, Fig. 2e-f). All examined garnet and two-pyroxene granulites show similar microstructural characteristics and exhibit well-defined foliation. The foliation is defined by distinct cm-scale compositional banding made of elongate, clinopyroxene-garnet or orthopyroxene-clinopyroxene stringers in a plagioclase matrix (Fig. 2a-d). The aspect ratios (a/b, where a - length, b - width) of these stringers vary from 3 to 24.

In all examined samples of granulites, garnet and pyroxene are relatively coarse-grained and feldspar grain size varies. Two generations of garnet, as described by Clarke et al. (2013), are present in garnet granulites. Type 1 of igneous origin is mostly sub-euhedral with grain diameter (d) of 0.3 to 1 mm and occurs in clusters with clinopyroxene (Fig. 2b). Type 2 garnet of metamorphic origin forms small euhedral grains (d: 0.2-0.5 mm) at the contact of stretched clinopyroxene clusters and plagioclase (Fig. 2c, d). Sub-euhedral pyroxene is 0.1 to 1 mm in diameter, with the majority of grains having d of 0.1-0.5 mm (Fig. 2c, d, f). Plagioclase is usually anhedral, with d of 0.1 to 1 mm. In samples from Breaksea Tops plagioclase shows straight grain boundaries, with multiple 120 ° triple junctions and weak undulose extinction (Fig. 2c). In granulites from Resolution Island plagioclase shows a bi-modal grain size distribution, with small grains surrounding large, ca. 1 mm in diameter grains (Fig. 2d). Large plagioclase grains show undulose extinction, subgrains and deformation twins (Fig. 2d).

The three eclogites examined in this study are mainly composed of granoblastic garnet and omphacite (Table 1, Fig. 2g). Garnet grains are 0.2 to 1 mm in diameter, with majority of grains in the range of 0.2 to 0.5 mm (Fig. 2h). Omphacite is slightly coarser-grained, with d from 0.3 to 1.5 mm, with the majority of grains with d between 0.3 and 0.7 mm (Fig. 2h). A distinct foliation defined by compositional banding of interlayered omphacite and garnet is present in eclogites (Fig. 2g, h).

4.2 Crystallographic orientation data

In garnet granulites, poles to (100) of plagioclase and clinopyroxene (diopside and omphacite) cluster in the foliation plane and normal to the lineation, poles to (010) are oriented normal to foliation plane, and poles to (001) are parallel or sub-parallel to the lineation (Fig. 3a). The strength of texture of plagioclase varies, with J-index from 2.3 to 6.7 for granulites from Breaksea Tops, and 2.8 to 4.7 for granulites from Resolution Island (Table 2). Omphacite and diopside show slightly lower J-index values that vary from 1.8 to 5.2 and 2.5 to 4.8, respectively (Table 2). Garnet texture shows a clustering of crystallographic planes around a single orientation, especially for (100) (Fig. 3a). This clustering is more pronounced for garnet in granulites from Resolution Island, where J-index ranges from 3.6 to 8.1 (Table 2). Garnets in granulites from Breaksea Tops show lower J-index values (1.3 to 4.6; Table 2), with the exception of sample BS05B, where texture is dominated by large (d ~ 6 mm) garnet phenocrysts (Appendix B).

In two-pyroxene granulites the poles to (100) of plagioclase cluster in the foliation plane, normal to lineation. Poles to (010) are oriented normal to the foliation plane, and those of (001) show clustering parallel to lineation (Fig. 3b). J-index of plagioclase varies from 4.4 to 6.9 (Table 2). Textures of diopside and enstatite in two-pyroxene granulite are characterized by clustering of poles to (001) parallel to lineation (Fig. 3b). Poles to (010) and (100) of diopside and (010) of enstatite do not show a distinctive texture (Fig. 3b). Poles to (100) in enstatite show clustering normal to the foliation plane (Fig. 3b). The J-indices of diopside and enstatite range from 2.0 to 6.7 and 3.1 to 8.2, respectively (Table 2).

In eclogites, omphacite texture is characterized by clustering of poles to (010) normal to foliation plane, and clustering of poles to (001) parallel to lineation (Fig. 3c). Poles to (100) are near randomly distributed. The J-index ranges from 2.7 to 3.9 (Table 2). Garnet does not show a distinctive texture (Fig. 3c), and the J-index varies from 1.2 to 2.4 (Table 2).

4.3. Seismic properties

4.3.1 Mean V_P and V_S

The results of the calculation of seismic properties applying the VRH and the AEH method are summarized in Table 3 and compared in Figure 4. We find the mean P-wave and S-wave velocities calculated for a given sample are nearly identical, despite using two different homogenisation methods (Table 3, Fig. 4a). Therefore, in the following we only refer to mean velocities calculated with the AEH method. The calculated mean P-wave velocities (MV_P) in garnet granulites ranges between the samples from 7.10 to 7.85 km s^{-1}, while MV_P in two-pyroxene granulites ranges from 6.85 to 6.87 km s^{-1} (Table 3). The mean S-wave velocities (MV_S) range from 4.06 to 4.46 km s^{-1} in garnet granulites, and from 3.96 to 3.98 km s^{-1} in two-pyroxene granulites (Table 3). In eclogites, MV_P and MV_S range from 8.47 to 8.54 and from 4.81 to 4.86 km s^{-1}, respectively.

MV_P and MV_S increase after recalculating the result to 600 MPa. In granulites, MV_P increases by 2.6-6.2 % and in eclogites MV_P increases by 2.4-2.9 % (Table 3). The largest increase in MV_P is observed for granulite BS04D and equals 0.47 km s^{-1} (Table 3). MV_S increases to a larger extent in eclogites than in granulites, 2.7-3.9 % vs. 0.3-3 %, respectively.

4.3.2 Seismic anisotropy in granulites

There is a noticeable difference in seismic anisotropy related to the method of calculation for analysed granulites (Fig. 4b, Table 3). The seismic anisotropy of P- and S-waves is significantly larger when the AEH calculation is applied (Table 3, Fig. 4b).

The range of P-wave anisotropy (AV_P) in garnet granulites calculated with the AEH method is 5.2-8.3 %, in contrast to only 0.9-2.9 % when calculated using the VRH method (Fig. 4b; Table 3). Similarly, the range of maximum S-wave anisotropy (AV_S) in garnet granulites is 3.4-6.6 % when calculated using the AEH, and only 1.0-3.6 % when calculated with the VRH (Fig. 4b; Table 3). The difference in AV_P and AV_S related to the calculation method is not as large in two-pyroxene granulites as in garnet granulites (Table 3, Fig. 4b). AV_P and AV_S are 5.9-6.0 % and 5.8-5.9 %, respectively, when calculated with the AEH, and 3.6-4.1 % and 3.7-3.9 % when calculated with the VRH (Fig. 4b, Table 3).

The two methods of homogenisation give two different distributions of V_P, AV_S, and V_{S1} polarization planes in garnet and two-pyroxene granulites (Fig. 5a-b, Appendix D). The P-wave velocity distribution in garnet and two-pyroxene granulites calculated with the AEH method shows orthorhombic symmetry, with slow velocities close to normal to the foliation, and a girdle of fast velocities in the foliation plane (Fig. 5a-b). In garnet granulites, V_P is fastest in the direction perpendicular to the lineation (sample Y-direction, Fig. 5a), while in two-pyroxene granulites the maximum velocity is sub-parallel to lineation (Fig. 5b). In both, AV_S is largest in the foliation plane, and for the direction showing largest anisotropy V_{S1} is polarized parallel to the plane of high AV_S (Fig. 5a-b).

The distribution of V_P, AV_S and orientation of Vs_1 polarization planes in garnet and two-pyroxene granulites calculated with the VRH average do not show a clear relationship with sample foliation or lineation (Fig. 5a-b). The V_P shows a girdle of slow velocities oriented ca. 45 ° to foliation, and travels the fastest in the directions sub-normal to the foliation (Fig. 5.5a-b). The AV_S shows two maxima in a girdle also oriented 45° to the foliation plane, with Vs_1 polarized almost perpendicular to a girdle of maximum AV_S (Fig. 5a-b).

4.3.3 Seismic anisotropy in eclogites

In contrast to garnet and two-pyroxene granulites, eclogites show similar seismic anisotropies for both methods of calculation, the AEH and the VRH (Fig. 4b). Calculated AV_P is smaller than 2 % and maximum AV_S is smaller than 1 % regardless the calculation method used (Fig. 4b, Table 3). Nevertheless, we observe a change in V_P and AV_S

distribution and V_{S1} polarization in the sample coordinates depending on the method used (Fig. 5c). While calculated with the AEH, P-waves are the fastest in the foliation plane and slowest in the direction normal to foliation, AV_S is largest in the foliation plane, with V_{S1} polarization planes oriented parallel to foliation (Fig. 5c). For the VRH calculation, V_P is also slowest normal to foliation, but their fast propagation is in the direction of lineation (Fig. 5c). The AV_S and V_{S1} polarization planes show a complex pattern, with multiple maxima (Fig. 5c).

5. Discussion

5.1 Impact of the microstructure on seismic properties

We use two methods of homogenisation to calculate seismic properties in this study: the VRH and the AEH-FE. The commonly used VRH average does not take into account the spatial arrangement of the minerals and assumes homogenous distribution of all the phases, whereas the AEH-FE method incorporates spatial arrangement of the minerals into calculation. Thus, the difference in seismic properties related to the application of the AEH-FE homogenisation can be used to estimate the effect of the distribution of the constitutive minerals on the wave propagation through the rock.

5.1.1 Garnet and two-pyroxene granulites

Assuming that all the minerals in garnet and two-pyroxene granulites are distributed randomly in the rock volume (the VRH average) we find the following relationships. P-wave velocity patterns in garnet granulites results from the combination of textures of plagioclase and clinopyroxene (Figs. 3 and 5). Plagioclase is characterized by high V_P anisotropy (AVp ~ 48 %), with slow P-wave velocities parallel to poles to (100) and (001), and fast velocities parallel to poles to (010) (Brown et al., 2006). Contrastingly, clinopyroxenes show fast V_P parallel to (100) and (001), and slow V_P parallel to poles to (010) (Bhagat et al., 1992; Collins and Brown, 1998). Those contrasting properties result in weak texture-related V_P anisotropy (~1-2 %, Table 3). The distribution of V_P shows the strongest link to plagioclase texture, due to its large modal percent and, in most cases, J-indices stronger than that of clinopyroxene (Tables 1 and 2, Figs. 3 and 5). Nearly isotropic garnet (Chai et al., 1997) does not contribute to the overall anisotropy of garnet granulites. V_P anisotropy in two-pyroxene granulites is higher than the anisotropy in the majority of garnet granulites (Table 3). In contrast to clinopyroxene, orthopyroxene is characterized by fast V_P parallel to poles to (010), which coincide with poles to (010) of plagioclase (Jackson et al., 2007). Therefore, textures of orthopyroxene and plagioclase superimpose to create a higher V_P anisotropy in two-pyroxene granulites. AV_S and the orientation of V_{S1} polarization planes are similar in garnet granulites and two-pyroxene granulites (Fig. 5). This suggests that the S-wave polarization is influenced mainly by texture of plagioclase and pyroxene, with little input from garnet. The orientation of the girdle that encompasses high AV_S resembles the symmetry of a theoretical gabbro modelled by Barruol and Mainprice (1993). Those authors have also attributed such seismic characteristic to the combination of properties of plagioclase and clinopyroxene, as orthopyroxene shows very low AV_S.

The high seismic anisotropy and modified distribution of V_P and AV_S in garnet and two-pyroxene granulites analysed with the AEH method suggests a strong microstructural impact on the seismic properties in these two rock types (Table 3). Due to compositional banding observed in garnet granulites and two-pyroxene granulites (Fig. 2a), the P-wave velocity markedly increases in the foliation plane and V_P distribution in the sample reference frame becomes orthorhombic (Fig. 5a-b). The comparison of the V_P distribution of two-pyroxene granulite and garnet granulites shows that the presence of garnet in the latter strengthens the orthorhombic character of P-wave velocities (Fig. 5a). Thus, the fast velocities around the sample Y-axis can be explained by the influence of garnet texture, and more precisely, an area of fast velocities between garnet (100) planes (Fig. 3). Interconnected stringers of garnet and pyroxene crystals dominate the signal originating from the layer of plagioclase, as garnet V_P in this direction is much faster than that of plagioclase. The girdle of high AV_S and V_{S1} polarization planes do not show a clear relationship with texture of any major mineral; it is now oriented parallel to the pyroxene ± garnet stringers that define foliation.

5.1.2 Eclogites

The magnitudes of P- and S-wave anisotropies in eclogites calculated with the AEH and the VRH are almost identical. In both cases, fast V_P propagates parallel to poles to (001) of omphacite, which are sub-parallel to the lineation (Figs. 3c and 5c). Slow V_P propagates parallel to poles to (100) of omphacite (Figs. 3c and 5c). The V_P distribution is only slightly modified by the microstructure, showing faster velocities in Y direction when calculated with the AEH method (Fig. 4).

The distribution of AV_S and orientation of S_1 polarization planes vary between the two methods to a larger degree. When VRH method is applied the AV_S maxima are difficult to link to texture of any of the contributing minerals (Fig. 5). When calculated with the AEH method the girdle of high AV_S and V_{S1} polarization planes are oriented parallel to mineral banding, as in granulites.

5.1.3 Effect of compositional banding versus texture

As shown in our data, a banded or foliated microstructure might not always be well represented by the VRH average. This is because such microstructure is in its nature anisotropic and the elastic response of a rock to the wave propagation might be closer to the isostress (Reuss) or isostrain (Voigt) bound rather than to their average. For example, in a compositionally banded medium composed of minerals of different density and elasticity, the rock response on the seismic wave propagating parallel to foliation (i.e. the compositional banding) will be closer to the Voigt (isostrain) average. Similarly, the response to the wave propagating perpendicular to the banding will be better represented by the Reuss (isostress) average. The orientation-related difference in wave speed will be especially large for the banded rocks composed of minerals with contrasting elastic constants and density, as their isostress and isostrain bounds are further apart. Therefore, even though we observe a well-defined foliation in eclogites (Fig. 2g-h) their seismic characteristics are only slightly modified by the spatial arrangement of garnets and pyroxenes in the rock mass. However, in garnet granulites where the density and elastic constants of plagioclase and pyroxene/garnet vary significantly the signature of compositional banding is strong.

It is necessary to point out that although we discuss a three dimensional microstructure, the EBSD data used provide only a two dimensional representation of grain boundary geometry that is projected into the third dimension. Thus, a potential error may arise that is related to the not quantified connectivity of minerals in the third dimension. However, all samples used show that the compositional banding is a planar and not linear features. Hence, anisotropy of the connectivity in the third dimension should only have a minor influence on our results.

5.2 Comparison with data from the literature

To date, majority of studies consider the mafic root of the lower crust to be isotropic due to a lack of strongly anisotropic minerals in granulite facies rocks (e.g., Lloyd et al., 2011). This seems to be confirmed by some laboratory measurements performed on granulites from the Kohistan Arc that show isotropic seismic velocities (Burlini et al., 2005; Kono et al., 2009). However, samples from these studies did not exhibit well-defined foliation and lineation. An AV_P of 6.4 % in mafic granulites from the same area was measured in the laboratory by Burlini et al. (2005). However, as the sample was collected from the transition zone between isotropic garnet-pyroxene granulites and foliated amphibolitic mylonites, it contained a large amount of hornblende exhibiting a strong texture. Since fastest V_P in these rocks were recorded parallel to lineation, which coincided with [001] axis of hornblende, the interpreted origin of anisotropy was due to an increasing amount of this mineral (Burlini et al., 2005). Nevertheless, Chroston and Simmons (1989) measured V_P in the garnet granulites cores from Kohistan and found AV_P of 5.6 and 5.7 % in two of the samples. Although a detailed microstructural description of the samples is not provided, some of the measured garnet granulites were "strongly banded" (Chroston and Simmons, 1989). Thus, the recorded anisotropies may be related to compositional banding.

To verify the accuracy of our result we compare the calculated mean velocities at room temperature and pressure of 600 MPa (Table 3) with previously published laboratory measurements for similar lithologies conducted at the same conditions (Fig. 6, Table E.1 in Appendix E). The mean seismic velocities calculated in this study are generally in a good agreement with previously published results (Fig. 6). Garnet and two-pyroxene granulites show slightly higher calculated than measured mean V_P and V_S velocities, while calculated and measured velocities of eclogites are comparable. The lower values of measured mean V_P and V_S velocities of granulites are most probably associated with the presence of secondary phases, porosity and/or microfractures in the samples; features that are not captured in EBSD analysis and, therefore, not incorporated into calculation. Secondary phases are likely to be present in feldspars, which might explain the very good correlation of measured and calculated mean seismic velocities in eclogites where feldspar is not present (Fig. 6).

5.3 Seismic anisotropy in foliated magmatic arc rocks: Insights from Fiordland, NZ

There is a question of the applicability of results calculated for the cm-scale microstructure to the km-scale rock mass. The AEH-FE method assumes that the microstructural geometry is periodic and all macroscale field variables are defined to have a periodic dependence on the microstructure. Thus, as long as the macroscale is much larger than the microscale (greater than three orders of magnitude), the bulk elastic properties of the rock can be evaluated using the AEH (Naus-Thijssen et al., 2011). Since foliation in granulites in Malaspina Pluton and Breaksea Tops defined by compositional banding is pervasive for at least hundreds of meters (Klepeis et al., 2016) this condition is satisfied in our case. On the other hand, a few-meters thick layers and pods of eclogites that occur in granulites will not likely be visible for naturally generated seismic waves.

The results presented in this study indicate that primary magmatic compositional banding and deformation related texture in mafic granulites are a potential source for anisotropy in the lower crustal rocks. Especially, the substantial shear wave splitting observed in the foliation plane in granulites may contribute to the seismic signal received at the surface. What is more, the S_1 foliation observed in Malaspina Pluton and Breaksea Orthogneiss is generally gently to steeply dipping (35-80°; Klepeis et al., 2016). The zone of steeply dipping foliations is 6 km wide (Klepeis et al., 2016). Thus, shear waves travelling vertically to the surface along S_1 foliation planes can undergo a substantial splitting (Barruol and Mainprice, 1993).

Most importantly, S_1 in Malaspina Pluton and Breaksea Orthogneiss is believed to resemble the original orientation of the magma flow during the intrusion emplacement only weakly reshaped during the subsequent deformation (Klepeis et al., 2016). In addition, based on study of the angular relationships of the garnet-rich veins in the northern part of WFO, the whole terrain experienced only minimal tilting during the exhumation (Daczko et al., 2001). This suggests that the microstructures observed in Fiordland are most likely present in the roots of present-day magmatic arcs, such as Papua and New Guinea Arc. Thus, the S-wave delay time interpretations in this setting should take into consideration the possible impact of layered intrusions on shear wave splitting. Similarly, the foliation-induced P-wave anisotropy, if neglected, might result in under-, or overestimation of V_P in the regions with shallowly and steeply dipping foliation, respectively.

We have not considered the effect of the increasing temperature on seismic velocities as would be the case in the natural geotectonic setting at the base of the magmatic arc. Of all the analysed minerals, the seismic properties of plagioclase are most impacted by the increasing temperature. Due to phase transformation, i.e. order-disorder transition at 400 °C in plagioclase, increasing temperature lowers V_P and V_S in this mineral (Kono et al., 2006). This might further increase the seismic anisotropy of garnet and two-pyroxene granulites, as the contrast between seismic velocities in plagioclase and pyroxene/garnet will be even larger.

6. Conclusions

We investigated the influence of compositional banding on seismic properties of rocks. The examples include foliated garnet and two-pyroxene granulites and eclogites from high-P and T mafic plutons of Western Fiordland Orthogneiss (Breaksea Orthogneiss and Malaspina

Pluton) that represent the base of an overthickened magmatic arc. Applying the asymptotic expansion homogenisation (AEH) method combined with finite element (FE) modelling that incorporates the spatial arrangement of minerals into analysis, we find a substantial P- and S-wave anisotropy (5-8% and 3-7%, respectively) in garnet granulites and two-pyroxene granulites. Significant shear wave splitting for S-waves travelling parallel to the foliation plane has also been determined in these rocks. These properties are not possible to detect applying the commonly used Voigt-Reuss-Hill average. We conclude the apparent seismic anisotropy originates from the compositional banding of plagioclase versus pyroxene ± garnet, minerals that exhibit contrasting elastic constants and density, without a necessary contribution from mineral textures. These results are directly transferable to other rocks that exhibit compositional banding with significant differences in density and elastic constants between bands. The distribution of V_P and AV_S in eclogites is also affected by the presence of garnet-clinopyroxene banding; however, due to a small contrast in density and elastic constants of constitutive minerals, their anisotropy is very low.

The generally intermediate to steeply dipping S_1 foliation that produces anisotropy in Breaksea Orthogneiss and Malaspina Pluton is pervasive at a scale of hundreds of meters. S_1 foliation has been interpreted as primarily magmatic with little tectonic overprint and the WFO experienced only minimal tilting during the exhumation. Consequently, we expect the presence of similar structures in plutons at the base of present day magmatic arcs and the data obtained in this study has direct implications for the interpretation of the seismic signal within this geotectonic setting.

Acknowledgements

The analytical data were obtained using instrumentation funded by DEST Systemic Infrastructure Grants, ARC LIEF, NCRIS, industry partners and Macquarie University. All the analyses were performed at the Geochemical Analysis Unit (GAU), in the Department of Earth and Planetary Sciences at Macquarie University, Australia. We thank David Adams for his support during SEM-based analyses. This work was supported by the Australian Research Council (project DP120102 and FT1101100070). We acknowledge Tim Chapman and Geoffrey Clarke for their field-based cooperation and sharing geochemical data. We thank the editor, Sarah Brownlee, and the anonymous reviewer for their comments that helped us to improve this article. We also thank Christopher Gerbi, David Mainprice and Bradley Hacker for their comments at the earlier stage of this study.

Tables

Table 1. Modal abundance of minerals in analysed rock samples estimated based on EBSD analysis and calculated densities. Mineral abbreviations after Kretz (1983).

Rock type	Sample no.	Density (g/cm^3)	Qtz	Pl	Kfs	Prg	Grt	Di	Omp	En	Ap	Ilm	Rt
two-pyroxene granulite	RS16A	2.90		54	10	1		18		13	1	3	
	RS10A	2.90	1	51	10	4		19		11		3	
garnet granulite	BS06B	3.03	3	56	4		22		14		1		1
	BS05B	3.08		50	4		22		22		1		1
	BS02A	3.11	4	39	7	2	25		21		1		1
	RS14A	3.13	5	40	7		30	18					1
	BS03C	3.14	5	33	8	1	28		25				
	BS04D	3.16	2	43		1	24		27		1		1
	BS04C	3.22	6	29	7		35		22		1		1
	RS09B	3.28		28		2	53	16			2		
	RS09A	3.40		42		2	45	10			2		1
eclogite	BS12C	3.55		1		4	54		37		1	1	1
	BS12D	3.55		1		3	55		38		1	1	1
	BS17B	3.58				7	50		41		1		

Table 2. J-indices estimated for ODFs of major rock forming minerals. All data points are included. Mineral abbreviations after Kretz (1983).

Rock type	Sample no.	J-index				
		Pl	Grt	Omp	Di	En
two-pyroxene granulite	RS16A	6.9			6.7	8.2
	RS10A	4.4			2.0	3.1
garnet granulite	BS06B	2.3	3.4	2.2		
	BS05B	4.8	38.0*	3.6		
	BS02A	6.7	4.6	5.2		
	RS14A	4.0	5.7		2.5	
	BS03C	4.7	1.3	2.7		
	BS04D	5.4	3.8	4.7		
	BS04C	4.7	3.1	1.8		
	RS09B	2.8	8.1		4.8	
	RS09A	4.7	3.6		4.2	
eclogite	BS12C		1.2	3.3		
	BS12D		2.4	2.7		
	BS17B		1.2	3.9		

* attributed to a large garnet porphyroclast

Table 3. Densities, and P- and S-wave velocities and anisotropies calculated from the EBSD data and elastic constants using VRH average with AEH correction (AEH) and simple VRH average (VRH). Anisotropy is calculated using the formula A = 200(Vmax-Vmin)/(Vmax-Vmin). Mean $V_P = (V_{P max} + V_{P min})/2$, Mean $V_S = (V_{S1 max} + V_{S2 min})/2$. Velocities are recalculated to 600 MPa applying Hashin-Shtrikmann bounds (Abers et al. 2016).

		V_P				V_S		V_{S1}			V_{S2}			V_P	V_S
Sample	Method	Min	Max	Mean	A	Mean	A	Min	Max	A	Min	Max	A	at 600 MPa	
		(km/s)			(%)	(km/s)	%	(km/s)		(%)	(km/s)		(%)	Mean (km/s)	
RS16A	AEH	**6.65**	**7.05**	**6.85**	**5.93**	**3.98**	**5.91**	**3.89**	**4.11**	**5.40**	**3.85**	**4.01**	**4.27**	**7.22**	**3.99**
	VRH	6.79	7.04	6.91	3.64	4.00	3.66	3.95	4.08	3.44	3.92	4.01	2.07		
RS10A	AEH	**6.66**	**7.07**	**6.87**	**6.04**	**3.96**	**5.83**	**3.90**	**4.08**	**4.56**	**3.85**	**4.03**	**4.62**	**7.21**	**3.99**
	VRH	6.76	7.04	6.90	4.10	3.98	3.91	3.95	4.06	2.80	3.90	4.02	3.18		
BS06B	AEH	**6.86**	**7.34**	**7.10**	**6.66**	**4.06**	**5.87**	**3.97**	**4.18**	**5.33**	**3.94**	**4.06**	**2.87**	**7.47**	**4.16**
	VRH	7.02	7.13	7.08	1.50	4.03	1.73	4.03	4.07	1.09	3.99	4.04	1.27		
BS05B	AEH	**7.01**	**7.49**	**7.25**	**6.62**	**4.15**	**6.11**	**4.06**	**4.28**	**5.35**	**4.01**	**4.14**	**3.09**	**7.65**	**4.23**
	VRH	7.12	7.31	7.21	2.72	4.10	2.27	4.10	4.15	1.16	4.04	4.12	1.98		
BS02A	AEH	**7.10**	**7.51**	**7.31**	**5.53**	**4.17**	**5.16**	**4.08**	**4.28**	**4.76**	**4.06**	**4.22**	**3.84**	**7.62**	**4.26**
	VRH	7.19	7.35	7.27	2.26	4.13	3.56	4.13	4.20	1.87	4.05	4.19	3.35		
RS14A	AEH	**7.10**	**7.56**	**7.33**	**6.32**	**4.18**	**4.98**	**4.15**	**4.29**	**3.48**	**4.07**	**4.30**	**5.57**	**7.52**	**4.22**
	VRH	7.19	7.33	7.26	1.97	4.13	1.90	4.14	4.18	0.99	4.09	4.16	1.65		
BS03C	AEH	**7.24**	**7.63**	**7.43**	**5.21**	**4.24**	**4.99**	**4.14**	**4.35**	**4.80**	**4.14**	**4.27**	**3.16**	**7.70**	**4.34**
	VRH	7.28	7.45	7.36	2.25	4.18	2.77	4.18	4.24	1.45	4.12	4.22	2.33		
BS04D	AEH	**7.13**	**7.59**	**7.36**	**6.22**	**4.24**	**6.62**	**4.22**	**4.39**	**3.88**	**4.10**	**4.29**	**4.60**	**7.82**	**4.37**
	VRH	7.22	7.53	7.37	4.26	4.22	3.31	4.19	4.31	2.71	4.14	4.23	2.18		
BS04C	AEH	**7.37**	**7.78**	**7.57**	**5.39**	**4.33**	**5.69**	**4.22**	**4.45**	**5.30**	**4.20**	**4.35**	**3.51**	**7.77**	**4.40**
	VRH	7.43	7.63	7.53	2.67	4.27	2.73	4.25	4.34	2.03	4.21	4.29	1.98		
RS09A	AEH	**7.18**	**7.80**	**7.49**	**8.26**	**4.28**	**5.87**	**4.23**	**4.43**	**4.46**	**4.13**	**4.33**	**4.78**	**7.86**	**4.37**
	VRH	7.35	7.57	7.46	2.92	4.24	2.63	4.22	4.31	2.16	4.17	4.25	1.95		
RS09B	AEH	**7.65**	**8.05**	**7.85**	**5.17**	**4.46**	**3.37**	**4.44**	**4.54**	**2.29**	**4.37**	**4.47**	**2.24**	**8.09**	**4.55**
	VRH	7.71	7.78	7.75	0.93	4.40	0.98	4.39	4.42	0.84	4.37	4.40	0.71		
BS17B	AEH	**8.41**	**8.53**	**8.47**	**1.45**	**4.81**	**0.85**	**4.80**	**4.83**	**0.77**	**4.79**	**4.81**	**0.44**	**8.72**	**5.00**
	VRH	8.38	8.53	8.45	1.80	4.80	0.63	4.79	4.81	0.42	4.78	4.80	0.48		
BS12D	AEH	**8.47**	**8.61**	**8.54**	**1.66**	**4.86**	**0.71**	**4.86**	**4.88**	**0.47**	**4.84**	**4.87**	**0.47**	**8.75**	**5.00**
	VRH	8.46	8.58	8.52	1.37	4.85	0.56	4.84	4.87	0.54	4.84	4.85	0.29		
BS12C	AEH	**8.46**	**8.59**	**8.53**	**1.45**	**4.86**	**0.77**	**4.85**	**4.88**	**0.68**	**4.84**	**4.86**	**0.43**	**8.73**	**4.99**
	VRH	8.46	8.58	8.52	1.40	4.85	0.73	4.84	4.87	0.62	4.83	4.86	0.58		

	Data source	Sample no.	Density (g/cm^3)	V_P Mean (km/s)	V_S
garnet granulite	Chroston and Simmons, 1989	P008	3.29	7.67	4.20
	Chroston and Simmons, 1989	P012	3.42	7.95	4.52
	Chroston and Simmons, 1989	P013	3.37	7.35	4.12
	Chroston and Simmons, 1989	P016	3.18	7.74	4.14
	Miller and Christensen, 1994	J6-2820	3.21	7.51	4.25
	Burlini et al. 2005	protolith	3.00	6.96	-
	Kono et al., 2009	PH332X	3.19	7.68	4.24
	Kono et al., 2009	PH333D	3.18	7.28	4.00
	Almqvist et al., 2013	K-7	3.27	7.24	-
two-pyroxene granulite	Manghnani et al., 1974	12	3.09	7.12	3.94
	Manghnani et al., 1974	13	3.12	7.02	3.76
	Manghnani et al., 1974	16	3.28	7.29	4.13
	Christensen and Fountaine, 1975	Italy	3.09	7.48	4.04
	Chroston and Simmons, 1989	P030	2.98	6.85	3.83
	Chroston and Simmons, 1989	P032	3.03	6.77	3.73
	Chroston and Simmons, 1989	P033	3.01	7.14	3.91
	Chroston and Simmons, 1989	P036	2.96	6.88	3.76
	Chroston and Simmons, 1989	P108	2.94	7.14	3.89
	Chroston and Simmons, 1989	P115	2.94	6.86	3.79
	Kono et al., 2009	PH335A	3.01	7.29	3.93
	Kono et al., 2009	PH332Y	3.02	7.37	3.97
eclogite	Kern et al., 2002	XG98-15	3.44	8.11	4.70
	Kern et al., 2002	MB98-02	3.59	8.57	4.90
	Kern et al., 2002	MB98-03	3.47	8.33	4.71
	Kern et al., 2002	MB 98-04	3.52	8.48	4.80
	Kern et al., 2002	MB 98-08	3.51	8.38	4.76
	Kern et al., 2002	MB 98-19	3.62	8.64	4.93
	Wang et al., 2009	B270	3.53	8.50	-
	Wang et al., 2009	B295	3.71	8.53	-

Table E.1 (in Appendix E) Data used to create Figure 6.

Figures and figure captions

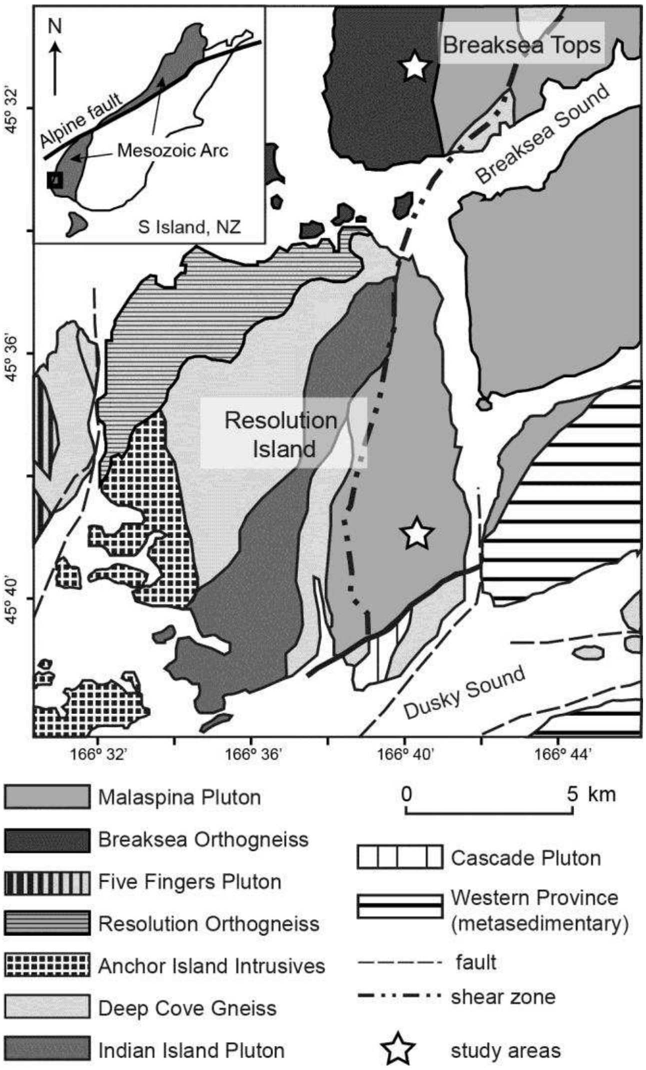

Figure 1. Sample localities shown on the geological map of the Resolution Island (Mt. Clerke samples) and Breaksea Sound area (Breaksea Tops samples) (modified from Allibone et al. (2009)). Inset shows the location of the study areas with respect to the Southern Island, New Zealand.

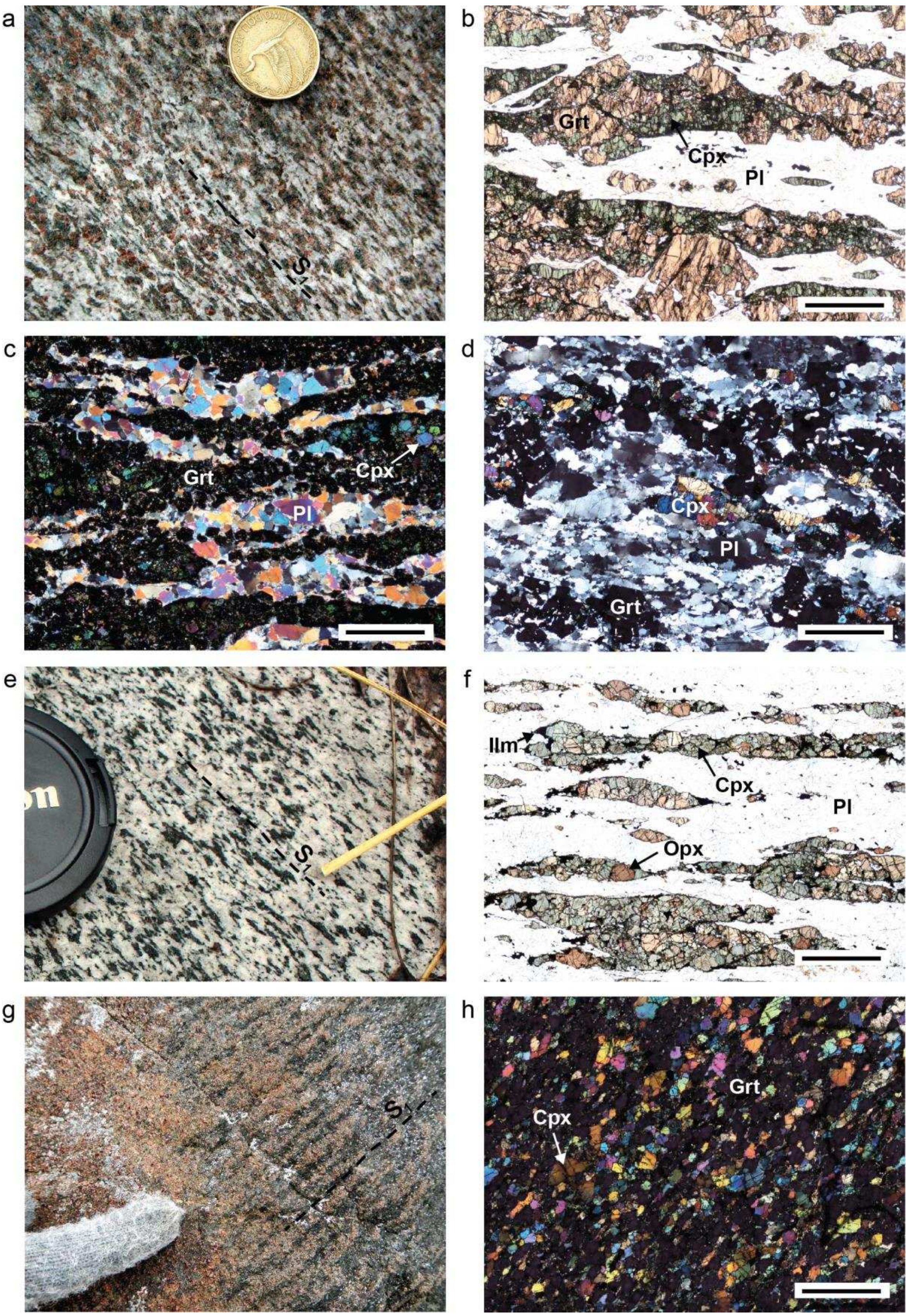

Figure 2. Field photographs (a, e, g) and plain (PPL) and cross-polarized (XPL) microphotographs (b-d, f, h) of representative examples of granulites and eclogites examined

in this study; note distinct compositional banding in all samples; scale bar represents 250 µm. a) garnet-diopside granulite, Resolution Island; b) garnet-omphacite stringers in plagioclase matrix, garnet granulite BS04C, PPL; c) euhedral garnet at plagioclase-omphacite contacts, equilibrated grain boundaries in plagioclase with multiple 120 ° triple junctions, garnet granulite BS03C, XPL, thick section; d) garnet-dominated garnet-diopside stringers in garnet granulite, plagioclase shows bimodal grain size distribution, undulose extinction and deformation twins, garnet granulite RS14A, XPL; e) foliated two-pyroxene granulite, Resolution Island; f) elongated, fish-like omphacite-enstatite clusters form foliation in two-pyroxene granulite, RS10A, PPL; g) foliated eclogite, Breaksea Tops; h) medium-grained omphacite and garnet in eclogite BS12C, XPL.

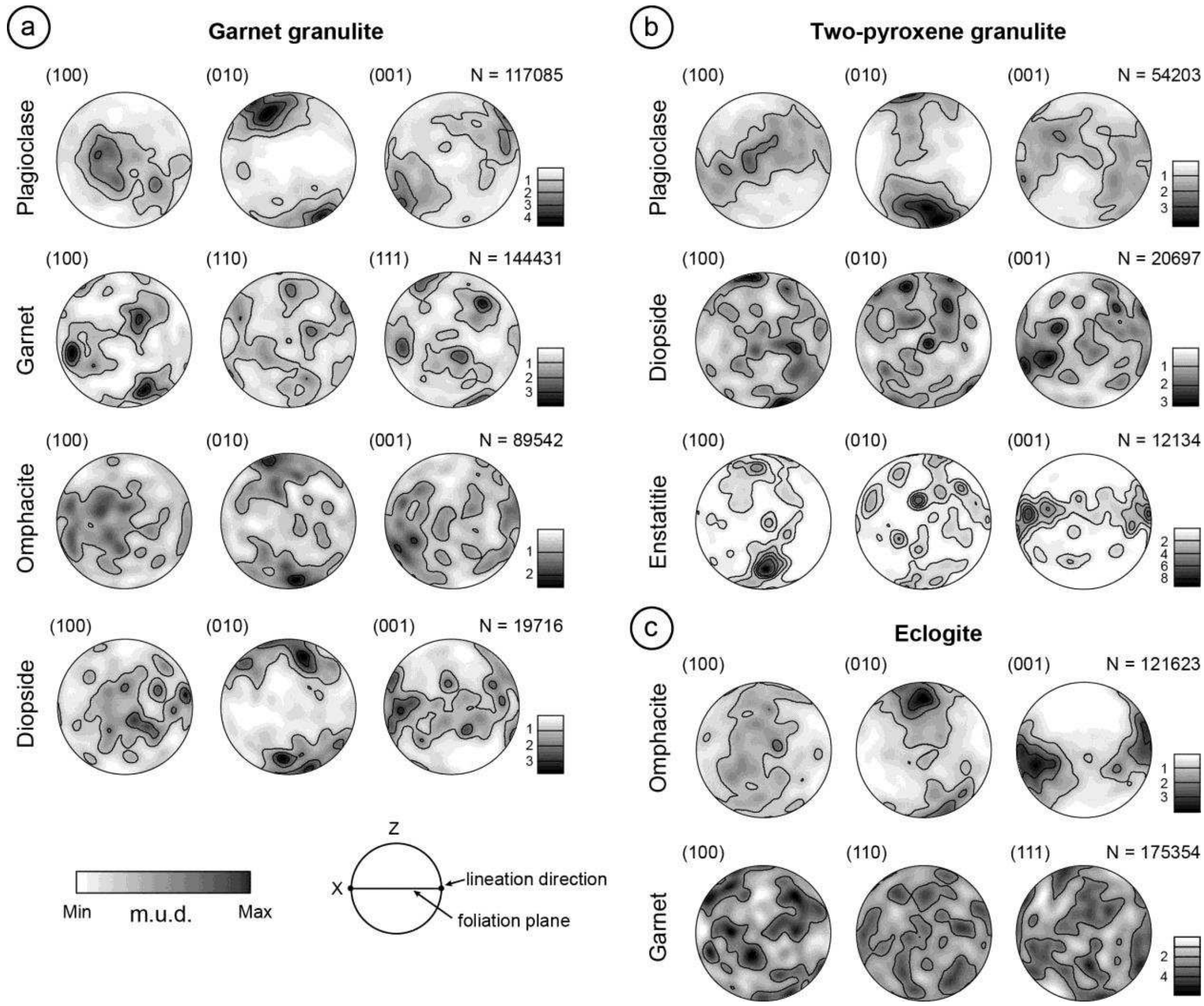

Figure 3. Representative textures of major phases in analysed rock samples; lower hemisphere, equal area pole figures, half-width is 15 ° and cluster size is 11 °. Contours are multiples of uniform distribution (m.u.d.) of 1, 2, etc. N represents the number of analysed points. a) garnet granulite: plagioclase, garnet and omphacite – BS04C, diopside – RS14A; b) two-pyroxene granulite RS10A, c) eclogite BS12C.

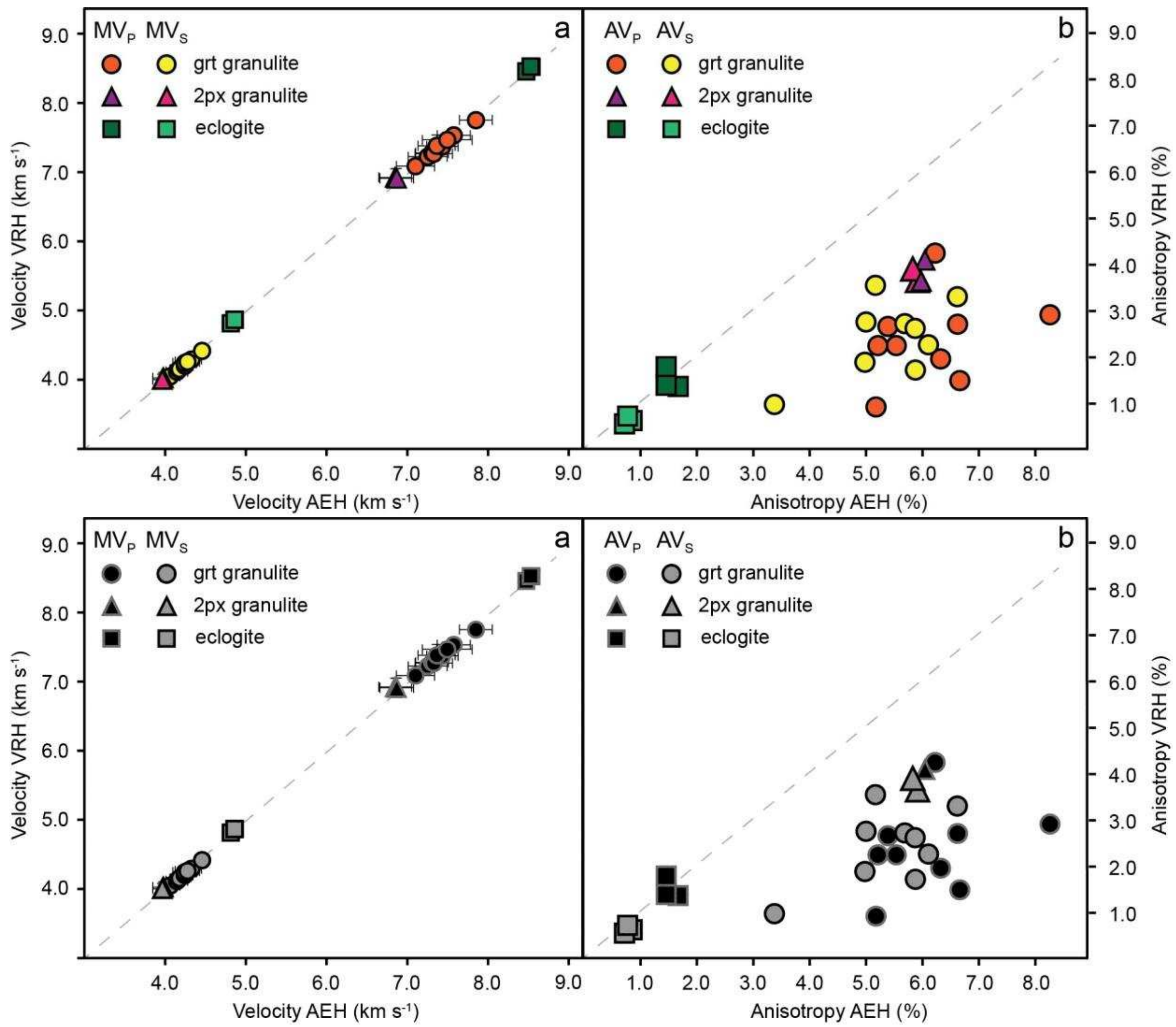

Figure 4. A comparison of mean seismic velocities (a) and seismic anisotropies (b) calculated with the two different methods of homogenisation: VRH and AEH (see text for details of methods used); dashed lines represent unity; bars marking mininmum and maximum velocities are shown unless there are within the size of the symbol used.

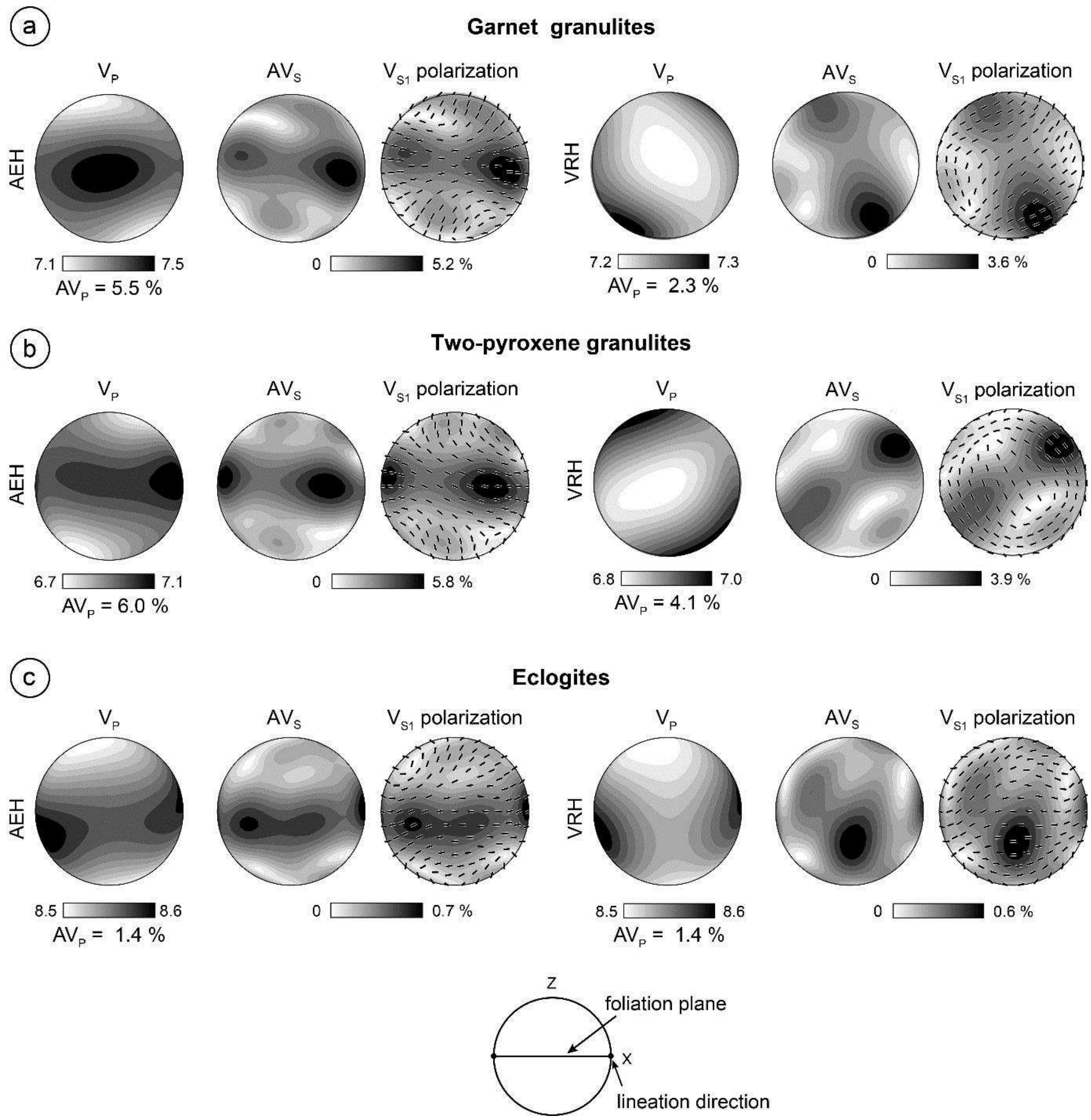

Figure 5. Representative P-wave velocities, V_S anisotropy and the orientation of V_{S1} polarization planes for the two different homogenisation methods: the AEH and the VRH (see text for details); lower hemisphere, equal area pole figures; note V_{S2} polarization planes are oriented perpendicular to those of V_{S1}. a) garnet granulite BS02A; b) two-pyroxene granulite RS10A, c) eclogite BS12C.

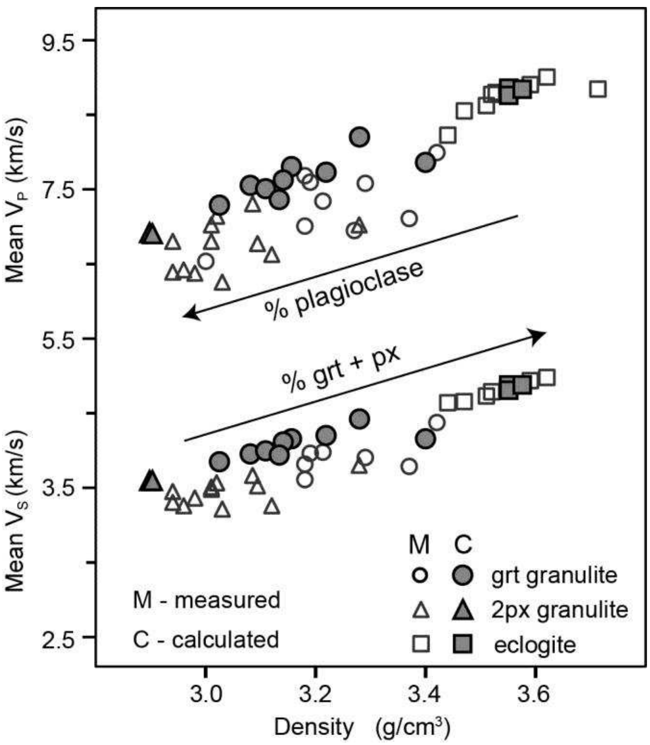

Figure 6. Calculated mean P- and S-wave velocities and density of granulites and eclogites from New Zealand (this study; filled symbols) at 600 MPa (Table 3) compared with velocities measured at 600 MPa and room temperature for similar lithologies (Manghnani et al., 1974; Christensen and Fountain, 1975; Chroston and Simmons, 1989; Miller and Christensen, 1994; Kern et al., 2002; Burlini et al., 2005; Kono et al., 2009; Wang et al., 2009; Almqvist et al., 2013; for data see Table E.1 in Appendix E).

References

Abers, G.A., Hacker, B.R., 2016. A MATLAB toolbox and Excel workbook for calculating the densities, seismic wave speeds, and major element composition of minerals and rocks at pressure and temperature. Geochemistry, Geophysics, Geosystems 17, 616-624. doi: 10.1002/2015GC006171

Aleksandrov, K., Ryzhova, T., 1961. Elastic properties of rock-forming minerals: I Pyroxenes and amphiboles. Acad Sci USSR Bull, Geophys Ser, 1165-1168.

Aleksandrov, K., Ryzhova, T., 1962. Elastic properties of rock-forming minerals: III feldspars. Acad Sci USSR Bull, Geophys Ser 2, 129-131.

Allibone, A.H., Jongens, R., Turnbull, I.M., Milan, L.A., Daczko, N.R., De Paoli, M.C., Tulloch, A.J., 2009. Plutonic rocks of western Fiordland, New Zealand: field relations, geochemistry, correlation, and nomenclature. New Zealand Journal of Geology and Geophysics 52, 379-415. doi: 10.1080/00288306.2009.9518465

Almqvist, B.S.G., Burg, J.P., Berger, J., Burlini, L., 2013. Seismic properties of the Kohistan oceanic arc root: Insights from laboratory measurements and thermodynamic modeling. Geochemistry Geophysics Geosystems 14, 1819-1841. doi: 10.1002/ggge.20125

Backus, G.E., 1962. Long-wave elastic anisotropy produced by horizontal layering. Journal of Geophysical Research 67, 4427-4440.

Baker, D.W., Carter, N.L., 1972. Seismic velocity anisotropy calculated for ultramafic minerals and aggregates. Flow and fracture of rocks, 157-166.
Barruol, G., Mainprice, D., 1993. A quantitative evaluation of the contribution of crustal rocks to the shear-wave splitting of teleseismic SKS waves. Physics of the Earth and Planetary Interiors 78, 281-300. doi: 10.1016/0031-9201(93)90161-2
Bhagat, S.S., Bass, J.D., Smyth, J.R., 1992. Single-crystal elastic properties of omphacite-C2/c by Brillouin spectroscopy. Journal of Geophysical Research: Solid Earth 97, 6843-6848. doi: 10.1029/92JB00030
Brown, J., Abramson, E., Angel, R., 2006. Triclinic elastic constants for low albite. Physics and Chemistry of Minerals 33, 256-265.
Bunge, H.J., 1982. Texture Analysis in Materials Science. Butterworth-Heinemann, London. doi: 10.1016/B978-0-408-10642-9.50006-4
Burlini, L., Arbaret, L., Zeilinger, G., Burg, J.-P., 2005. High-temperature and pressure seismic properties of a lower crustal prograde shear zone from the Kohistan Arc, Pakistan. Geological Society, London, Special Publications 245, 187-202. doi: 10.1144/gsl.sp.2005.245.01.09
Chai, M., Brown, J.M., Slutsky, L.J., 1997. The elastic constants of a pyrope-grossular-almandine garnet to 20 Gpa. Geophysical Research Letters 24, 523-526.
Chapman, T., Clarke, G.L., Daczko, N.R., 2016. Crustal differentiation in a thickened Arc - Evaluating Depth Dependences. Journal of Petrology 57, 595-620. doi: 10.1093/petrology/eqw022
Chapman, T., Clarke, G.L., Daczko, N.R., Piazolo, S., Rajkumar, A., 2015. Orthopyroxene–omphacite- and garnet–omphacite-bearing magmatic assemblages, Breaksea Orthogneiss, New Zealand: Oxidation state controlled by high-P oxide fractionation. Lithos 216–217, 1-16. doi: 10.1016/j.lithos.2014.11.019
Cheng, B., Zhao, D., Cheng, S., Ding, Z., Zhang, G., 2016. Seismic tomography and anisotropy of the Helan-Liupan tectonic belt: Insight into lower crustal flow and seismotectonics. Journal of Geophysical Research: Solid Earth 121, 2608-2635. doi: 10.1002/2015JB012692
Christensen, N.I., Fountain, D.M., 1975. Constitution of the lower continental crust based on experimental studies of seismic velocities in granulite. Geological Society of America Bulletin 86, 227-236.
Christoffel, E., 1877. Ueber die Fortpflanzung von Stössen durch elastische feste Körper. Annali di Matematica Pura ed Applicata (1867-1897) 8, 193-243.
Chroston, P.N., Simmons, G., 1989. Seismic velocities from the Kohistan volcanic arc, northern Pakistan. Journal of the Geological Society 146, 971-979. doi: 10.1144/gsjgs.146.6.0971
Clarke, G., Daczko, N., Miescher, D., 2013. Identifying relic igneous garnet and clinopyroxene in eclogite and granulite, Breaksea Orthogneiss, New Zealand. Journal of Petrology 54, 1921-1938. doi: 10.1093/petrology/egt036
Collins, M.D., Brown, J.M., 1998. Elasticity of an upper mantle clinopyroxene. Physics and Chemistry of Minerals 26, 7-13. doi: 10.1007/s002690050156
Daczko, N., Clarke, G., Klepeis, K., 2001. Transformation of two-pyroxene hornblende granulite to garnet granulite involving simultaneous melting and fracturing of the lower crust, Fiordland, New Zealand. Journal of Metamorphic Geology 19, 549-562. Doi: 10.1046/j.0263-4929.2001.00328.x
De Paoli, M., Clarke, G., Klepeis, K., Allibone, A., Turnbull, I., 2009. The eclogite–granulite transition: mafic and intermediate assemblages at Breaksea Sound, New Zealand. Journal of Petrology 50, 2307-2343. doi: 10.1093/petrology/egp078

Hielscher, R., Schaeben, H., 2008. A novel pole figure inversion method: specification of the MTEX algorithm. Journal of Applied Crystallography 41, 1024-1037.
Hill, R., 1952. The elastic behaviour of a crystalline aggregate. Proceedings of the Physical Society 65, 349.
Jackson, J.M., Sinogeikin, S.V., Bass, J.D., 2007. Sound velocities and single-crystal elasticity of orthoenstatite to 1073K at ambient pressure. Physics of the Earth and Planetary Interiors 161, 1-12. doi: 10.1016/j.pepi.2006.11.002
Karato, S.I., Wu, P., 1993. Rheology of the upper mantle: A synthesis. Science 260, 771-778.
Kern, H., Jin, Z., Gao, S., Popp, T., Xu, Z., 2002. Physical properties of ultrahigh-pressure metamorphic rocks from the Sulu terrain, eastern central China: implications for the seismic structure at the Donghai (CCSD) drilling site. Tectonophysics 354, 315-330. doi: 10.1016/S0040-1951(02)00339-6
Klepeis, K.A., Schwartz, J., Stowell, H., Tulloch, A., 2016. Gneiss domes, vertical and horizontal mass transfer, and the initiation of extension in the hot lower-crustal root of a continental arc, Fiordland, New Zealand. Lithosphere, L490. 491. doi: 10.1130/L490.1
Kono, Y., Ishikawa, M., Arima, M., 2006. Laboratory measurements of P-and S-wave velocities in polycrystalline plagioclase and gabbronorite up to 700° C and 1 GPa: Implications for the low velocity anomaly in the lower crust. Geophysical Research Letters 33. doi: 10.1029/2006GL026526
Kono, Y., Ishikawa, M., Harigane, Y., Michibayashi, K., Arima, M., 2009. P- and S-wave velocities of the lowermost crustal rocks from the Kohistan arc: Implications for seismic Moho discontinuity attributed to abundant garnet. Tectonophysics 467, 44-54. doi: 10.1016/j.tecto.2008.12.010
Lakshtanov, D.L., Sinogeikin, S.V., Bass, J.D., 2007. High-temperature phase transitions and elasticity of silica polymorphs. Physics and Chemistry of Minerals 34, 11-22.
Lloyd, G., Butler, R., Casey, M., Tatham, D., Mainprice, D., 2011. Constraints on the seismic properties of the middle and lower continental crust. Geological Society, London, Special Publications 360, 7-32. doi: 10.1144/Sp360.2
Mainprice, D., Nicolas, A., 1989. Development of shape and lattice preferred orientations: application to the seismic anisotropy of the lower crust. Journal of Structural Geology 11, 175-189. doi: 10.1016/0191-8141(89)90042-4
Manghnani, M.H., Ramananantoandro, R., Clark, S.P., 1974. Compressional and shear wave velocities in granulite facies rocks and eclogites to 10 kbar. Journal of Geophysical Research 79, 5427-5446.
Milan, L.A., Daczko, N.R., Clarke, G.L., Allibone, A.H., 2016. Complexity of In-situ zircon U–Pb–Hf isotope systematics during arc magma genesis at the roots of a Cretaceous arc, Fiordland, New Zealand. Lithos 264, 296-314. doi: 10.1016/j.lithos.2016.08.023
Miller, D.J., Christensen, N.L., 1994. Seismic signature and geochemistry of an island arc: A multidisciplinary study of the Kohistan accreted terrane, northern Pakistan. Journal of Geophysical Research: Solid Earth 99, 11623-11642.
Mortimer, N., Hoernle, K., Hauff, F., Palin, J.M., Dunlap, W.J., Werner, R., Faure, K., 2006. New constraints on the age and evolution of the Wishbone Ridge, southwest Pacific Cretaceous microplates, and Zealandia–West Antarctica breakup. Geology 34, 185-188. doi: 10.1130/g22168.1
Moschetti, M., Ritzwoller, M., Lin, F., Yang, Y., 2010. Seismic evidence for widespread western-US deep-crustal deformation caused by extension. Nature 464, 885-889. doi: 10.1038/nature08951
Naus-Thijssen, F.M.J., Goupee, A.J., Vel, S.S., Johnson, S.E., 2011. The influence of microstructure on seismic wave speed anisotropy in the crust: computational analysis of

quartz-muscovite rocks. Geophysical Journal International 185, 609-621. doi: 10.1111/j.1365-246X.2011.04978.x

Reuss, A., 1929. Berechnung der fließgrenze von mischkristallen auf grund der plastizitätsbedingung für einkristalle. Zeitschrift für Angewandte Mathematik und Mechanik 9, 49-58.

Sha, M.C., Li, Z., Bradt, R.C., 1994. Single-crystal elastic constants of fluorapatite, Ca5F (PO4)3. Journal of Applied Physics 75, 7784-7787. doi: 10.1063/1.357030

Siegesmund, S., Kern, H., Vollbrecht, A., 1991. The effect of oriented microcracks on seismic velocities in an ultramylonite. Tectonophysics 186, 241-251. doi: 10.1016/0040-1951(91)90361-U

Stowell, H., Parker, K.O., Gatewood, M., Tulloch, A., Koenig, A., 2014. Temporal links between pluton emplacement, garnet granulite metamorphism, partial melting and extensional collapse in the lower crust of a Cretaceous magmatic arc, Fiordland, New Zealand. Journal of Metamorphic Geology 32, 151-175. doi: 10.1111/jmg.12064

Vel, S.S., Cook, A.C., Johnson, S.E., Gerbi, C., 2016. Computational homogenization and micromechanical analysis of textured polycrystalline materials. Computer Methods in Applied Mechanics and Engineering 310, 749-779. doi: 10.1016/j.cma.2016.07.037

Voigt, W., 1928. Lehrbuch der Kristallphysik B. G. Teubner, Berlin and Leipzig.

Wachtman Jr, J., Tefft, W., Lam Jr, D., 1962. Elastic constants of rutile (TiO2). Journal of Research of the National Bureau of Standards 66, 465-471.

Walker, A.M., Wookey, J., 2012. MSAT—A new toolkit for the analysis of elastic and seismic anisotropy. Computers & Geosciences 49, 81-90. doi: 10.1016/j.cageo.2012.05.031

Wang, Q., Burlini, L., Mainprice, D., Xu, Z., 2009. Geochemistry, petrofabrics and seismic properties of eclogites from the Chinese Continental Scientific Drilling boreholes in the Sulu UHP terrane, eastern China. Tectonophysics 475, 251-266. doi: 10.1016/j.tecto.2008.09.027

Weidner, D.J., Ito, E., 1985. Elasticity of MgSiO3 in the ilmenite phase. Physics of the Earth and Planetary Interiors 40, 65-70. doi: 10.1016/0031-9201(85)90006-8

Figure (high-resolution)
Click here to download Figure (high-resolution): 1_Fig_NZmap.eps

Figure (high-resolution)
Click here to download Figure (high-resolution): 2_Microstructures_BW.tif

Figure (high-resolution)

Click here to download Figure (high-resolution): 4_AEH_VHR comparison_BW.eps

Figure (high-resolution)
Click here to download Figure (high-resolution): 5_Seismic properties.eps

Table

Click here to download Table: CyprychEtAl - Tables.xlsx

Table 1. Modal abundance of minerals estimated based on EBSD analysis (area %) and calculated densities of analysed rock samples. Mineral abbreviations after Kretz (1983).

Rock type	Sample no.	Density (g/cm^3)	Qtz	Pl	Kfs	Prg	Grt	Di	Omp	En	Ap	Ilm	Rt
two-pyroxene granulite	RS16A	2.90		54	10	1		18		13	1	3	
	RS10A	2.90	1	51	10	4		19		11		3	
garnet granulite	BS06B	3.03	3	56	4		22		14		1		1
	BS05B	3.08		50	4		22		22		1		1
	BS02A	3.11	4	39	7	2	25		21		1		1
	RS14A	3.13	5	40	7		30	18					1
	BS03C	3.14	5	33	8	1	28		25				
	BS04D	3.16	2	43		1	24		27		1		1
	BS04C	3.22	6	29	7		35		22		1		1
	RS09B	3.28		28		2	53	16			2		
	RS09A	3.40		42		2	45	10			2		1
eclogite	BS12C	3.55		1		4	54		37		1	1	1
	BS12D	3.55		1		3	55		38		1	1	1
	BS17B	3.58				7	50		41		1		

Supplementary material for online publication only
Click here to download Supplementary material for online publication only: Appendix B_EBSD maps.pdf

Supplementary material for online publication only

Click here to download Supplementary material for online publication only: Appendix D_seismic properties.pdf